

Stable Organic-Inorganic Hybrid Bismuth-Halide Monocrystalline Compounds With Adjustable Optoelectronic Properties

Xinru Hu

Guilin University of Technology

Jilin Wang (✉ jilinwang@glut.edu.cn)

Guilin University of Technology

Jian He

Guilin University of Technology

Guoyuan Zheng

Guilin University of Technology

Disheng Yao

Guilin University of Technology

Shuyi Mo

Guilin University of Technology

Nan Tian

Guilin University of Technology

Bing Zhou

Guilin University of Technology

Fei Long

Guilin University of Technology

Research Article

Keywords: Single crystal structure, Organic-inorganic hybrid, Bismuth (Bi) based hybrid compound, Hirshfeld surface analysis, Optical property and stability

Posted Date: August 6th, 2021

DOI: <https://doi.org/10.21203/rs.3.rs-746969/v1>

License:  This work is licensed under a Creative Commons Attribution 4.0 International License.

[Read Full License](#)

Abstract

Two kinds of novel organic-inorganic bismuth-halide hybrid monocrystalline compounds $(C_6H_5CH_2NH_3)_2BiCl_5$ and $(C_6H_5CH_2NH_3)BiI_4$ were synthesized and characterized. The crystal structure, intermolecular interaction, morphology, chemical groups and bonds, optical and thermal stability of the samples were systematically investigated through single crystal X-ray diffraction, Hirshfeld surface analysis, SEM, FTIR, TG and UV-vis diffuse reflectance spectra. The results indicated that $(C_6H_5CH_2NH_3)_2BiCl_5$ and $(C_6H_5CH_2NH_3)BiI_4$ crystals displayed a monoclinic system with the space group P21/c and P21/n at room temperature, respectively. These materials showed strong absorption in the ultraviolet and visible light regions, resulting in very low E_g , which could be continuously adjustable from 1.67 eV to 3.21 eV by changing the halogen ratio. In addition, these hybrid materials also exhibited good thermal stability. The decomposition temperature of $(C_6H_5CH_2NH_3)_2BiCl_5$ and $(C_6H_5CH_2NH_3)BiI_4$ were 260°C and 300°C respectively. Therefore, these organic-inorganic bismuth-halide hybrid compounds have excellent development potential in the field of solar cell research.

Introduction

In the past 12 years, organic-inorganic hybrid perovskite materials have achieved remarkable results in solar cells[1–3]. The photoelectric conversion efficiency of perovskite solar cells (PSCs) has soared from 3.8–25.5%[4, 5], which is close to the efficiency of commercialized silicon solar cells[6], and much superior to other photovoltaic technologies. At present, most perovskite materials are based on lead-halide (PbX_2) compounds as a reactant, which contain a heavy metal element. This is harmful to environment and humans' health[7]. In addition, the instability of lead-based perovskite materials is another huge challenge for commercialization of PSCs[8]. These materials decompose easily under exposure of heat, moisture and oxygen, which increase the risk of lead leakage[9]. Therefore, the replacement of lead with environmental-friendly metals is a key issue for the development of PSCs.

Bismuth-based (Bi^{3+}) organic-inorganic hybrid materials have attracted much attention from their optoelectronic properties to device performance. Firstly, Bi^{3+} and Pb^{2+} have the same electronic arrangement, small ionic radius gap, and closed electronegativity to form a relatively stable perovskite structure[10]. Furthermore, both the Bi-based perovskite material and the Pb-based perovskite material have adjustable optical bandgaps and simple solution processability[11]. Moreover, Bi-based organic-inorganic hybrid materials are more stable than lead-based organic-inorganic hybrid materials[12]. Therefore, the Bi-based perovskite is a promising substitute for Pb-based perovskite materials. However, the large band gap of Bi-based perovskites leads to the weakened photoelectric conversion efficiency of the Bi-based PSCs.

Herein, we propose the synthesis of two kinds of bismuth-based monocrystalline perovskites. The crystal structure, intermolecular interaction, morphology, chemical groups and bonds characterization were

systematically investigated in detailed. In addition, the optical properties and thermal stability for the $(C_6H_5CH_2NH_3)_2BiCl_5$ and $(C_6H_5CH_2NH_3)BiI_4$ compounds were also investigated.

Experiments

2.1. Compound preparation

All starting reagents were of analytical grade and used without any further purification. Bismuth (III) oxide (Bi_2O_3) were purchased from Macklin Chemistry Co. Ltd. Benzylamine (99%), Hydroiodic acid (HI) (wt%=47%). Hydrochloric acid (HCl) (wt%=36%) were purchased from Xilong Chemistry Co. Ltd. Diethyl ether and ethanol were obtained from Sinopharm Chemical Reagent Co. Ltd. The $C_6H_5CH_2NH_3X$ ($X = Cl, I$) salts were obtained by the reaction of benzylamine and HX in an ice bath with continuous stirring for 2 hours. The mixed solution was placed in an oven and dried at $60^\circ C$ for 12 hours. In the next step, the solid product was washed several times with ether and ethanol. Finally, the $C_6H_5CH_2NH_3X$ was dried in a vacuum at $60^\circ C$ for 12 h.

2.1.1. Synthesis of $(C_6H_5CH_2NH_3)_2BiCl_5$

Bi_2O_3 (2330 mg, 5 mmol) and $C_6H_5CH_2NH_3Cl$ (718 mg, 5 mmol) were dissolved in HCl (5 mL) and DMF (2 mL), and the solution was stirred at room temperature for 30 min. The white single crystals were obtained by evaporating the mixed solution in an environment of $60^\circ C$ for 7 days. 2.1.2. Synthesis of $(C_6H_5CH_2NH_3)BiI_4$

Bi_2O_3 (2330 mg, 5 mmol) and $C_6H_5CH_2NH_3I$ (1175 mg, 5 mmol) were dissolved in HI (10 mL), and the solution was stirred at room temperature for 30 min. The solution was placed in an oven at $100^\circ C$ for 10 hours and red crystals were formed.

Results And Discussion

3.1 Morphology and crystal structure

Figure 1(a₁)-(b₁) and **Fig. 1(a₂)-(b₂)** were the digital photographs and SEM images of the $(C_6H_5CH_2NH_3)_2BiCl_5$ and $(C_6H_5CH_2NH_3)BiI_4$ single crystals, respectively. The $(C_6H_5CH_2NH_3)_2BiCl_5$ possesses granular shape, while $(C_6H_5CH_2NH_3)BiI_4$ showed simple prismatic shape. In order to analyze the crystal structure of the single crystal, single crystal diffraction and powder X-ray diffraction (PXRD) were carried out at room temperature. The crystal structures of single crystals were shown in **Fig. 1(a₃)-(b₃)**. At the same time, the single crystal X-ray diffraction data of $(C_6H_5CH_2NH_3)_2BiCl_5$ and $(C_6H_5CH_2NH_3)BiI_4$ were summarized in Table 1. Owing to different coordinate axes chosen, the $(C_6H_5CH_2NH_3)_2BiCl_5$ crystals belongs to the monoclinic system and P21/c space group, while the $(C_6H_5CH_2NH_3)BiI_4$ crystals the monoclinic system and P21/n space group. The crystal structures of the

anisotropic displacement parameters and other structural information have been deposited with the Cambridge Crystallographic Data Centre under the registration number CCDC 1886951, 1883198, respectively.

Table 1
Crystal data and structure refinement for $(C_6H_5CH_2NH_3)_aBi_bX_c$

Empirical formula	$(C_6H_5CH_2NH_3)_2BiCl_5$	$(C_6H_5CH_2NH_3)BiI_4$
Formula weight (g mol ⁻¹)	602.55	1649.48
Crystal system	monoclinic	monoclinic
Space group	P2 ₁ /c	P2 ₁ /n
α(°)	90	90
β(°)	97.195(3)	90.455(4)
γ(°)	90	90
a(Å)	13.5528(4)	12.4166(6)
b(Å)	12.8311(3)	7.8330(4)
c(Å)	12.1296(3)	15.9264(7)
Volume(Å ³)	2092.68(9)	1548.95(12)
Z	4	2
Density (g cm ⁻³)	1.912	3.537
Diffractometer/scan	Agilent G8910A CCD	Agilent G8910A CCD
Radiation, λ (Å),	0.71073	0.71073
Monochromator θ range (°)	6.772 to 58.546	6.564 to 58.13
Unique reflections	15133	11205
F(0 0 0)	1144.0	1416.0
Index ranges	-18 ≤ h ≤ 17, -17 ≤ k ≤ 15, -16 ≤ l ≤ 14	-15 ≤ h ≤ 16, -10 ≤ k ≤ 10, -15 ≤ l ≤ 20
GOF on F ²	1.036	1.138
Absorption correction	Spherical harmonics	Spherical harmonics
Data/restraints/parameters	5052/0/201	3672/0/120
Final R indexes [I > 2σ (I)]	R ₁ = 0.0341, wR ₂ = 0.0664	R ₁ = 0.0379, wR ₂ = 0.0790
Final R indexes (all data)	R ₁ = 0.0591, wR ₂ = 0.0777	R ₁ = 0.0487, wR ₂ = 0.0849
Min/max (q/e Å ⁻³)	1.44/-1.34	1.89/-1.07

$(C_6H_5CH_2NH_3)_2BiCl_5$ presented typical two-dimensional (2D) structure. The basic structural unit of $(C_6H_5CH_2NH_3)_2BiCl_5$ compound consisted of benzylammonium cation and corner-sharing $[BiCl_6]$ octahedra. Each Bi^{3+} in the structure was surrounded by six halogen anions Cl^- to form an inorganic octahedral structure. The octahedrons were connected by sharing two halogen anions Cl^- . $[C_6H_5CH_2NH_3]^+$ cations occupied the gaps of the octahedral, and each inorganic layer $[BiCl_6]^-$ connected two adjacent organic layers $[C_6H_5CH_2NH_3]^+$ to form an alternating organic-inorganic hybrid structure. The organic group and the inorganic octahedron were connected by unequal $N-H\cdots Cl$ hydrogen bonds, combined with weak van der Waals interactions to form a two-dimensional perovskite structure.

While $(C_6H_5CH_2NH_3)BiI_4$ displayed typical one-dimensional (1D) structure which consisted of $[C_6H_5CH_2NH_3]^+$ cations and infinite linear anionic chains $[BiI_6]^-$. In the crystal structure, each Bi^{3+} is surrounded by six halogen anions I^- to form an inorganic octahedral structure. And the adjacent octahedrons were connected by sharing two anion I^- to form a one-dimensional chain. The organic group $[C_6H_5CH_2NH_3]^+$ occupied the octahedral gap which was connected with the inorganic octahedral structure through the $N-H\cdots I$ hydrogen bond to form an organic-inorganic hybrid structure.

To investigate the purity of two types of single crystals, the PXRD were performed as shown in **Fig. 2(a₁) (b₂)**. It could be seen from the figure that the experimental test pattern was roughly consistent with the theoretical simulation pattern which indicated the reliability of refined single crystal structures and purity phase of those crystals.

3.2. Hirshfeld surface analysis

To research the various interactions that lead to the crystal structure in detail, Hirshfeld surfaces[13] and fingerprint plots were generated for the $(C_6H_5CH_2NH_3)_aBi_bX_c$ compound based on the crystallographic information file (CIF) using CrystalExplorer[14]. Hirshfeld surfaces enable the visualization of intermolecular interactions with different colours and colour intensity representing short or long contacts and indicating the relative strength of the interactions.

It was a significant advance in understanding the crystal packing behavior[15] which using the 2D-fingerprint plots and shape index to analysis the intermolecular interactions. The distance of the three-dimensional (3D) molecular Hirshfeld surfaces from surface to the nearest nucleus inside the surface was defined ' d_i' ', and the distance from surface to the nearest nucleus outside the surface was defined ' d_e' '[16]. The normalized contact distance (d_{norm}) is given by:

$$d_{norm} = \frac{d_i - r_i^{vdw}}{r_i^{vdw}} + \frac{d_e - r_e^{vdw}}{r_e^{vdw}} \quad (1)$$

' r_i^{vdw} ' and ' r_e^{vdw} ' were defined the van der Waals radii of the appropriate atoms, respectively. Graphical plots of the molecular Hirshfeld surfaces mapped with d_{norm} employ the red-white-blue colour scheme where red area represents the strongest contact, blue area indicates weaker contact.

The ' d'_i ', ' d'_e ', ' d'_{norm} ', shape index, curvedness curves mapping on Hirshfeld surface of $(C_6H_5CH_2NH_3)_2BiCl_5$ were shown in the **Fig. 3**. The fixed color scale in Fig. 3a₁-a₅ were 0.901 Å (red) ~ 2.879 Å (blue), 0.903 Å~2.972 Å, -0.416 Å~1.558 Å, -1.000 Å~1.000 Å, and - 4.000Å~0.400 Å respectively. The corresponding 2D fingerprint plot of $(C_6H_5CH_2NH_3)_2BiCl_5$ was as shown in Figure S1. Globally, the H...Cl/Cl...H intermolecular interactions had the largest contribution to the Hirshfeld surface, with percentage contributions of 46.2%(19.4%+26.8%). Owing to the molecular surface had large amount of hydrogen, the second most abundant interactions contribution was from H...H contacts with percentage of 34.8%. The remaining C...Cl/Cl...C, H...C/C...H, Cl...Cl, Bi...Cl/Cl...Bi, C...C intermolecular contacts of the Hirshfeld surface only contributes 0.2%, 12.9%, 1.6%, 3.4%, 0.8% respectively.

The ' d'_i ', ' d'_e ', ' d'_{norm} ', shape index and curvedness curves surfaces of compound $(C_6H_5CH_2NH_3)BiI_4$ were shown in the **Fig. 4**, the fixed color scale of 3D mapped surfaces were between 1.000 Å (red) ~ 2.940 (blue), 0.946 Å~2.823 Å, -0.356 Å~1.016 Å, -1.000 Å~1.000 Å, and - 4.000Å~4.000 Å respectively. Figure S2 provide us information about intermolecular interactions of 2D-fingerprint plots. The decomposition of the fingerprint plots show that H...I/ I...H contacts comprise 64% of the total Hirshfeld surface area for the molecule of $(C_6H_5CH_2NH_3)BiI_4$ which confirms significant of these interactions on structural stability. Furthermore, the proportion of H...H interactions to the tune of 12.2% in Hirshfeld surfaces of $(C_6H_5CH_2NH_3)BiI_4$ indicated that these contacts are the second most significant interaction. Apart from these above, the C...H /H...C, C...C, I...C/C...I,, I...I, Bi...H, Bi...I/I...Bi of the Hirshfeld surface only contributes 6.5%, 2.7%, 0.6%, 4.7%, 0.1%, 9.2% respectively.

According to the parameter analysis of the ' d'_i ', ' d'_e ', ' d'_{norm} ', shape index and curvedness curves of $(C_6H_5CH_2NH_3)_2BiCl_5$ and $(C_6H_5CH_2NH_3)BiI_4$, the ratios of the bonds and the interaction ratios between the elements are different because of the difference in halogens.

3.3. FT-IR Spectra study

In order to understand information about the organic group and inorganic framework of the compound $(C_6H_5CH_2NH_3)_aBi_bX_c$ in more detail, FT-IR spectroscopy were performed (Fig. 5). And the detailed assignments of vibrational models were listed in Table 2. Obviously, the peaks between 500-3500 cm^{-1} belong to the benzylamine ring, and those peaks below 500 cm^{-1} belong to the peak of (Bi-X) (X = Cl, I) [17]. The asymmetric and symmetric stretching bands of NH_3^+ were usually located at 3330 and 3080 cm^{-1} [18], respectively. In $(C_6H_5CH_2NH_3)_aBi_bX_c$, the NH_3^+ group interacts with the halide atoms through N-H...X hydrogen bonds. As seen from Table 2, the $\delta_{asym}(NH_3)$ and $\delta_{sym}(NH_3)$ modes are coupled with the C-C ring stretching mode. The CH_2 asymmetric and symmetric stretching modes are observed at 2849 to 2856 cm^{-1} and at 2764 cm^{-1} [19].

Table 2
Measured resonance frequencies of vibrational modes and peak assignments for the
 $(C_6H_5CH_2NH_3)_aBi_bX_c$

$(C_6H_5CH_2NH_3)_2BiCl_5$	$(C_6H_5CH_2NH_3)BiI_4$	Peak assignment
IR Wavenumbers (cm^{-1})	IR Wavenumbers (cm^{-1})	
3443	3443	$\nu_{asym}(NH_3^+)$
3117	3146	$\nu_{sym}(NH_3^+)$
2920	2920	$\nu_{asym}(CH_3)$
2849	2856	$\nu_{asym}(CH_2)$
2764	-	$\nu_{sym}(CH_2)$
1628	1628	$\delta_{asym}(NH_3) + \nu(C-C)ring$
1551	1558	$\delta_{sym}(NH_3) + \nu(C-C)ring$
1459	1445	$\delta_{sym}(CH_3) + \delta_{sym}(CH_2)$
1359	1374	$\nu_{asym}(C-N)$
1078	1057	$\beta(C-H)$
-	-	$\beta(C-H)$
1014	923	$\rho(NH_3)$
880	845	$\gamma(C-H)$
810	781	$\gamma(C-H)$
753	746	$\nu(C-C) + \beta(C-C-C)$
696	690	$\gamma(C-C-C)$
569	563	$\beta(C-C-C)$
484	478	$\nu_{asym}(Bi-X)$

v: stretching; δ : scissoring or bending; t:twisting; ρ : rocking; t: torsion; as: asymmetric, s:symmetric

3.4. Thermogravimetric analysis and stability

To investigate the mass loss behavior of each component of the $(C_6H_5CH_2NH_3)_aBi_bX_c$ single crystal materials in detail, the thermogravimetric curve were obtained from room temperature to 800°C. As

Fig. 6a shown, $(C_6H_5CH_2NH_3)_2BiCl_5$ exhibited one thermal events and was stable up to $260^\circ C$, all organic and inorganic compounds decompose completely at $350^\circ C$. And the $(C_6H_5CH_2NH_3)BiI_4$ is stable up to $300^\circ C$, decomposed completely at $410^\circ C$. In short, different halogens have different stability between Bi-X bonds, resulting in different stability of compounds.

3.5. Optical property

To calculate the optical band gap of $(C_6H_5CH_2NH_3)_aBi_bX_c$, UV-Visible absorption spectra were carried out, as shown in **Fig. 7**. The absorbance as a function of reflectance explained by Kubelka-Munk Eq. [20], the formula is as follows:

$$F(R) = \alpha = (1-R)^2/(2R) \quad (2)$$

where R represents the value of light reflectivity and α means the optical absorption coefficient.

According to the UV-vis spectrum, it could clearly observe that the absorption edge of $(C_6H_5CH_2NH_3)_2BiCl_5$, $(C_6H_5CH_2NH_3)BiI_4$ was located at about 440 nm, 890 nm which indicating that the band gap was 3.21 eV, 1.67 eV respectively. As the ionic radius of I^- is larger than that of Cl^- , the ultraviolet-visible absorption peak of $(C_6H_5CH_2NH_3)BiI_4$ is red-shifted compared to $(C_6H_5CH_2NH_3)_2BiCl_5$, resulting in an increase in the light absorption range[21–23]. Therefore, the band gaps of $(C_6H_5CH_2NH_3)BiI_4$ is smaller than the $(C_6H_5CH_2NH_3)_2BiCl_5$, the light absorption range of $(C_6H_5CH_2NH_3)BiI_4$ is wider than the $(C_6H_5CH_2NH_3)_2BiCl_5$. In summary, the $(C_6H_5CH_2NH_3)BiI_4$ have more application potential in light-emitting, Diodes (LEDs), photodetectors, lasers and other fields, compared to the $(C_6H_5CH_2NH_3)_2BiCl_5$.

Conclusions

Two kinds of novel single crystal materials $(C_6H_5CH_2NH_3)_aBi_bX_c$ ($X = Cl, I$) were successfully synthesized by different preparation methods. The $(C_6H_5CH_2NH_3)_2BiCl_5$ and $(C_6H_5CH_2NH_3)BiI_4$ crystals were demonstrated monoclinic system with the space group P21/c and P21/n at room temperature, respectively. These single crystals show various types of intermolecular interactions such as hydrogen bonding. The band gap values of $(C_6H_5CH_2NH_3)_2BiCl_5$ and $(C_6H_5CH_2NH_3)BiI_4$ decreased from 3.21 eV to 1.67 eV respectively. Simultaneously, the single crystal materials $(C_6H_5CH_2NH_3)_aBi_bX_c$ ($X = Cl, I$) was provided with high thermal stability which $(C_6H_5CH_2NH_3)_2BiCl_5$ and $(C_6H_5CH_2NH_3)BiI_4$ could be kept within $260^\circ C$ and $300^\circ C$ without decomposition respectively. In conclusion, the performance of $(C_6H_5CH_2NH_3)_aBi_bX_c$ ($X = Cl, I$) materials indicates its excellent development potential in the field of solar cell research.

Declarations

Funding

The authors acknowledge the financial support from National Natural Science Foundation of China (No.51972071), Guangxi Research Foundation for Science and Technology Base and Talent Special (No. AD19245175), Non-ferrous metals and materials processing new technology Ministry of education key laboratory open fund project (No.19AA-14), and Guangxi Distinguished Experts Special Fund (No.2019B06).

Declaration of Competing Interest

We declare that We have no known competing financial interests or personal relationships that could have appeared to influence the work reported in this paper.

Data availability

All data generated or analyzed during this study are included in this published article.

Authors' contributions

All authors contributed to the study conception and design. Xinru Hu, Jilin Wang, Fei Long performed material preparation, data collection, and analysis. Xinru Hu wrote the first draft of the manuscript and all authors commented on previous versions of the manuscript. All authors read and approved the final manuscript.

References

1. Li X-L, Li Z, Zhang G, Yang G-J (2020) Lead-free perovskite $[\text{H}_3\text{NC}_6\text{H}_4\text{NH}_3]\text{CuBr}_4$ with both a bandgap of 1.43 eV and excellent stability. *Journal of Materials Chemistry A* 8:5484–5488
2. Ji C, Wang P, Wu Z, Sun Z, Li L, Zhang J et al (2018) Inch-Size Single Crystal of a Lead-Free Organic-Inorganic Hybrid Perovskite for High-Performance Photodetector. *Adv Funct Mater* 28:1705467
3. Liu Y, Zhang Y, Yang Z, Ye H, Feng J, Xu Z et al (2018) Multi-inch single-crystalline perovskite membrane for high-detectivity flexible photosensors. *Nat Commun* 9:5302
4. Kojima A, Teshima K, Shirai Y, Miyasaka T (2009) Organometal halide perovskites as visible-light sensitizers for photovoltaic cells. *J Am Chem Soc* 131:6050–6051
5. Laboratory NRE, Best Research-Cell Efficiency Chart, <https://www.nrel.gov/pv/cell-efficiency.html>. NRE Laboratory, Best Research-Cell Efficiency Chart, <https://www.nrel.gov/pv/cell-efficiency.html>
6. Yoshikawa K, Kawasaki H, Yoshida W, Irie T, Konishi K, Nakano K et al (2017) Silicon heterojunction solar cell with interdigitated back contacts for a photoconversion efficiency over 26%. *Nature energy* 2:1–8
7. Ke W, Stoumpos CC, Kanatzidis MG (2019) “Unleaded” perovskites: status quo and future prospects of tin-based perovskite solar cells. *Adv Mater* 31:1803230
8. Ke W, Kanatzidis MG (2019) Prospects for low-toxicity lead-free perovskite solar cells. *Nat Commun* 10:1–4

9. Boyd CC, Cheacharoen R, Leijtens T, McGehee MD (2018) Understanding degradation mechanisms and improving stability of perovskite photovoltaics. *Chem Rev* 119:3418–3451
10. Wu C, Zhang Q, Liu G, Zhang Z, Wang D, Qu B et al (2020) From Pb to Bi: A Promising Family of Pb-Free Optoelectronic Materials and Devices. *Advanced Energy Materials* 10:1902496
11. Kou B, Zhang W, Ji C, Wu Z, Zhang S, Liu X et al (2019) Tunable optical absorption in lead-free perovskite-like hybrids by iodide management. *Chem Commun* 55:14174–14177
12. Lyu M, Yun J-H, Cai M, Jiao Y, Bernhardt PV, Zhang M et al (2016) Organic-inorganic bismuth (III)-based material: A lead-free, air-stable and solution-processable light-absorber beyond organolead perovskites. *Nano Research* 9:692–702
13. Spackman MA, Jayatilaka D (2009) Hirshfeld surface analysis. *CrystEngComm* 11:19–32
14. Adonin SA, Gorokh ID, Samsonenko DG, Novikov AS, Korolkov IV, Plyusnin PE et al (2019) Binuclear and polymeric bromobismuthate complexes: Crystal structures and thermal stability. *Polyhedron* 159:318–322
15. Dhifi M, Thabet S, Harchani A, Haddad A (2019) Synthesis, characterization, Hirshfeld surface analysis and theoretical calculation of new organic-inorganic hybrid material: $(C_4H_7N_2)_6[As_2W_{18}O_{62}] \cdot 4H_2O$. *J Iran Chem Soc* 16:777–784
16. Tahiri O, Kassou S, El Mrabet R, Belaaraj A (2019) Synthesis, Hirshfeld surface analysis, optical and electronic properties of the functional hybrid perovskite $[NH_3-(CH_2)_2-NH_3]CdCl_4$: a combined experimental and theoretical study. *Materials Research Express* 6:076301
17. Amamou W, Feki H, Chniba-Boudjada N, Zouari F (2014) Synthesis, crystal structure, vibrational properties and theoretical investigation of (N, N-dimethylbenzylammonium) trichlorocadmate (II). *J Mol Struct* 1059:169–175
18. Rached AB, Maalej W, Guionneau P, Daro N, Mhiri T, Feki H et al (2018) Synthesis, crystal structure, and vibrational and DFT simulation studies of benzylammonium dihydrogen phosphite. *J Phys Chem Solids* 123:150–156
19. Sajan D, Binoy J, Pradeep B, Krishna KV, Kartha V, Joe IH et al (2004) NIR-FT Raman and infrared spectra and ab initio computations of glycinium oxalate. *Spectrochimica Acta Part A: Molecular Biomolecular Spectroscopy* 60:173–180
20. Yang B, Mao X, Hong F, Meng W, Tang Y, Xia X et al (2018) Lead-free direct band gap double-perovskite nanocrystals with bright dual-color emission. *J Am Chem Soc* 140:17001–17006
21. Ye Y, Run X, Hai-Tao X, Feng H, Fei X, Lin-Jun W (2015) Nature of the band gap of halide perovskites ABX_3 (A = CH_3NH_3 , Cs; B = Sn, Pb; X = Cl, Br, I): First-principles calculations. *Chinese Physics B*. 24:116302
22. Ravi VK, Markad GB, Nag A (2016) Band edge energies and excitonic transition probabilities of colloidal $CsPbX_3$ (X = Cl, Br, I) perovskite nanocrystals. *ACS Energy Letters* 1:665–671
23. Hu X, Wang J, Mao W, Zheng G, Mo S, Tian N et al (2021) Synthesis, Crystal Structure, Optical Properties and Stability of New Bismuth-Based Organic-Inorganic Compounds $(C_6H_9N_2)_aBi_bX_c$ (X =

Figures

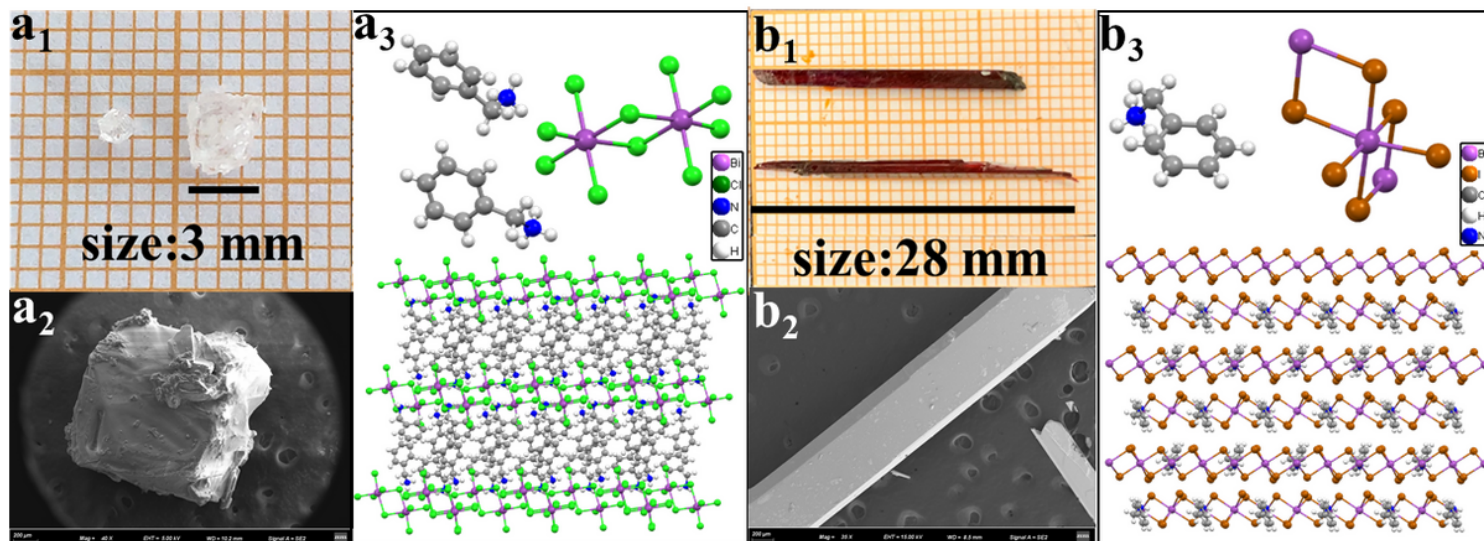


Figure 1

a1-The digital photograph of the (C₆H₅CH₂NH₃)₂BiCl₅ single crystal; b1-The digital photograph of the (C₆H₅CH₂NH₃)BiI₄ single crystal; a2-The SEM image of (C₆H₅CH₂NH₃)₂BiCl₅ single crystal; b2-The SEM image of (C₆H₅CH₂NH₃)BiI₄ single crystal; a3-The crystal structure of the (C₆H₅CH₂NH₃)₂BiCl₅; b3-The crystal structure of the (C₆H₅CH₂NH₃)BiI₄

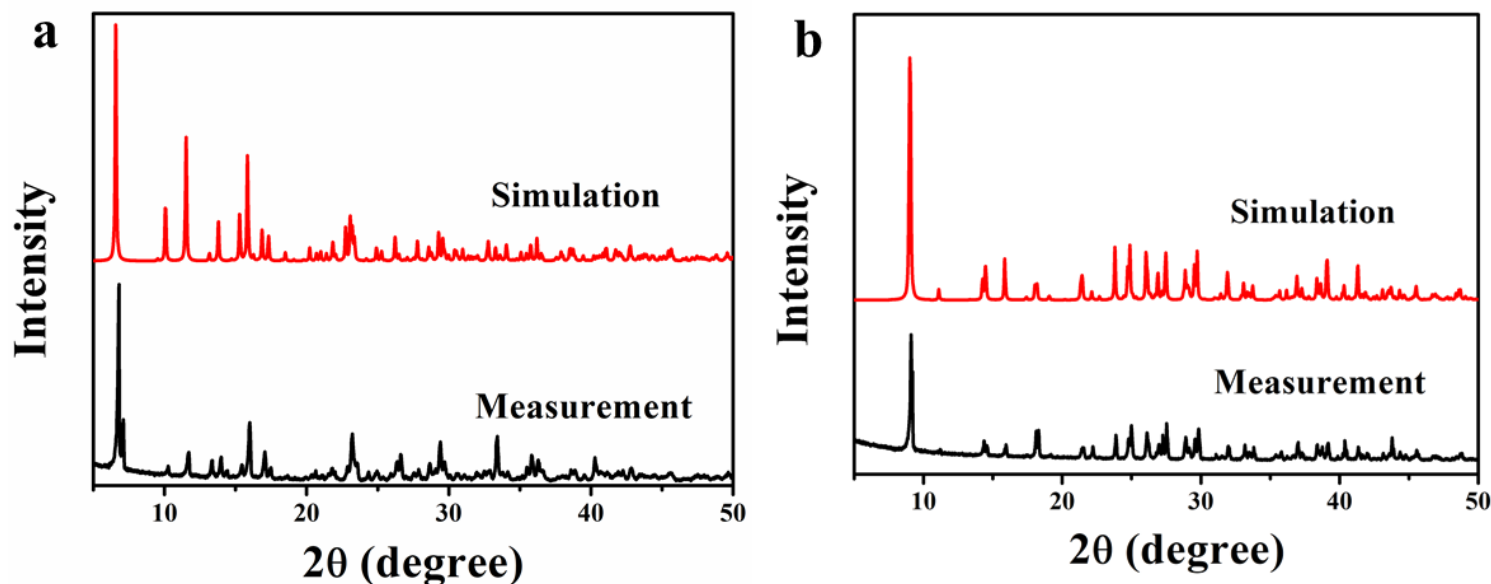


Figure 2

a1-Experimental powder PXRD and simulated PXRD patterns of (C₆H₈N₂)BiCl₅; b2-Experimental powder PXRD and simulated PXRD patterns of (C₆H₅CH₂NH₃)BiI₄

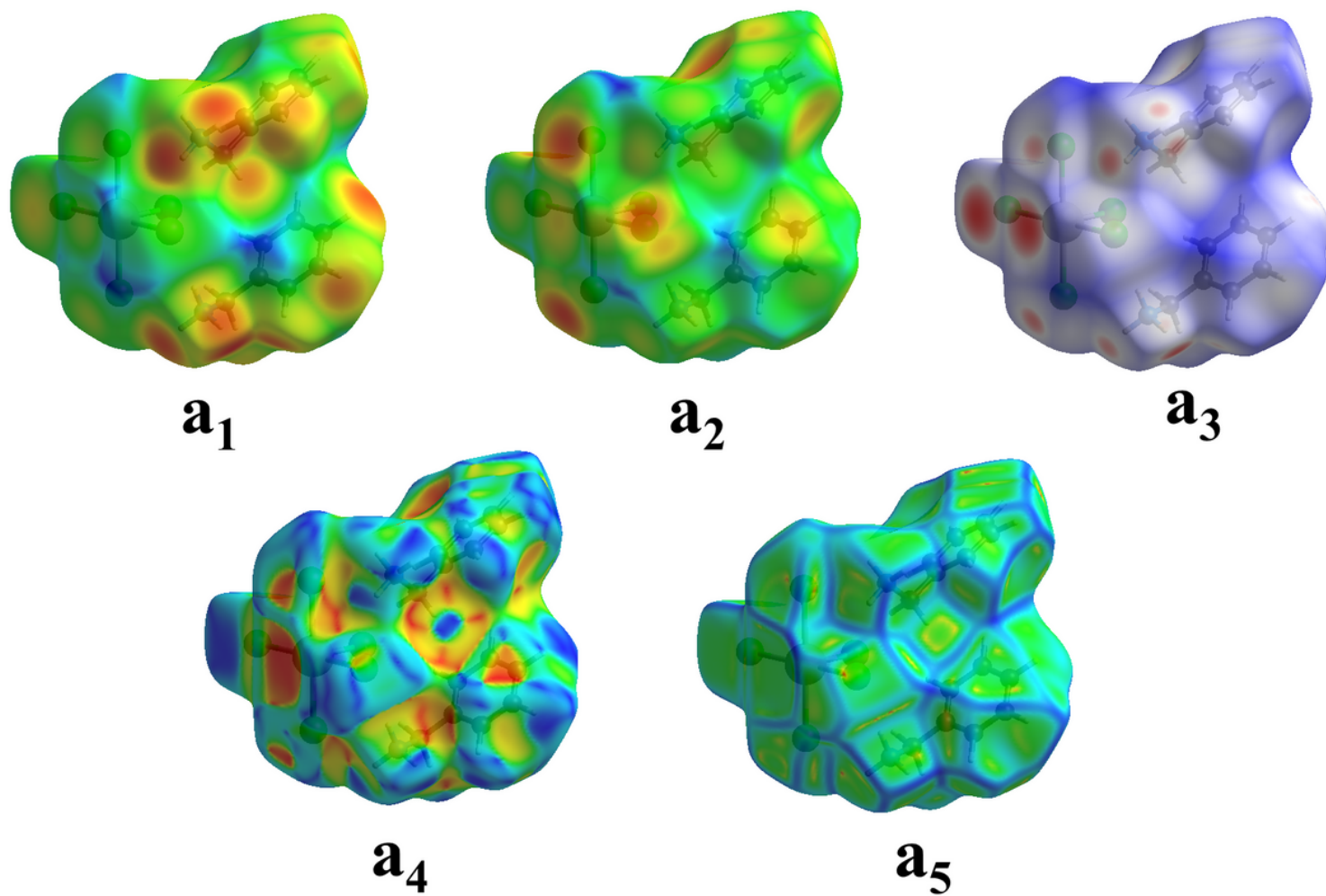


Figure 3

The Hirshfeld surface for $(C_6H_5CH_2NH_3)_2BiCl_5$ mapped with 'di', 'de', 'dnorm', shape index and curvedness curves

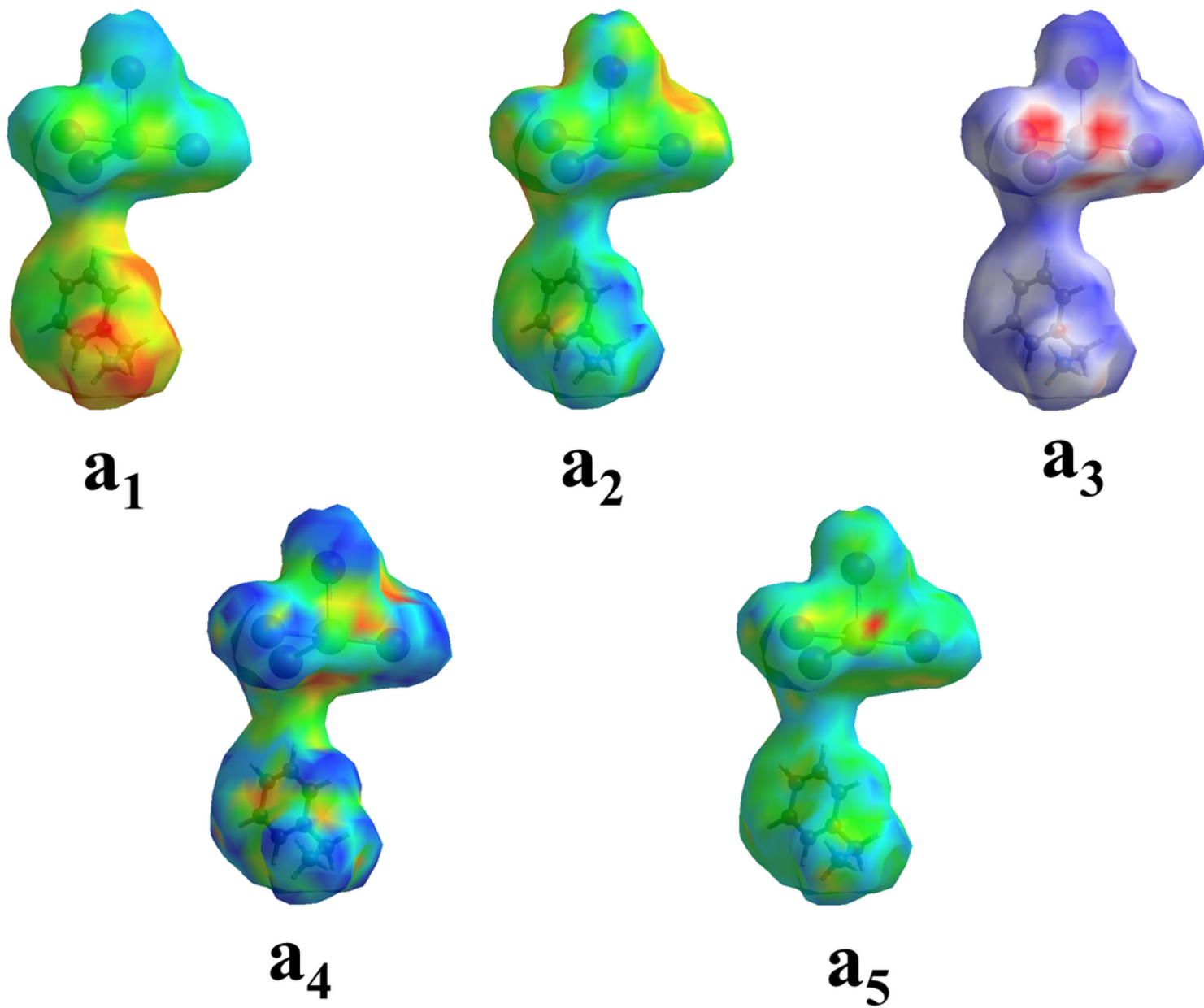


Figure 4

The Hirshfeld surface for $(C_6H_5CH_2NH_3)BiI_4$ mapped with 'di', 'de', 'dnorm', shape index and curvedness curves

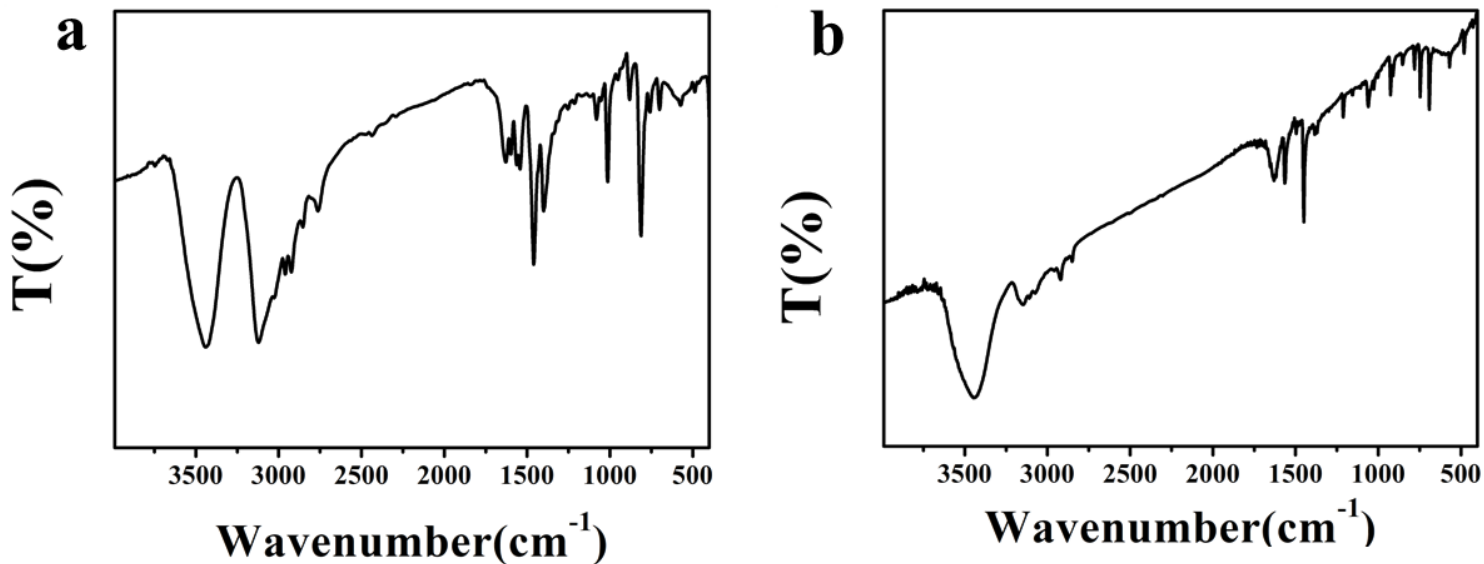


Figure 5

a-IR spectrum of $(C_6H_5CH_2NH_3)_2BiCl_5$; b-IR spectrum of $(C_6H_5CH_2NH_3)BiI_4$

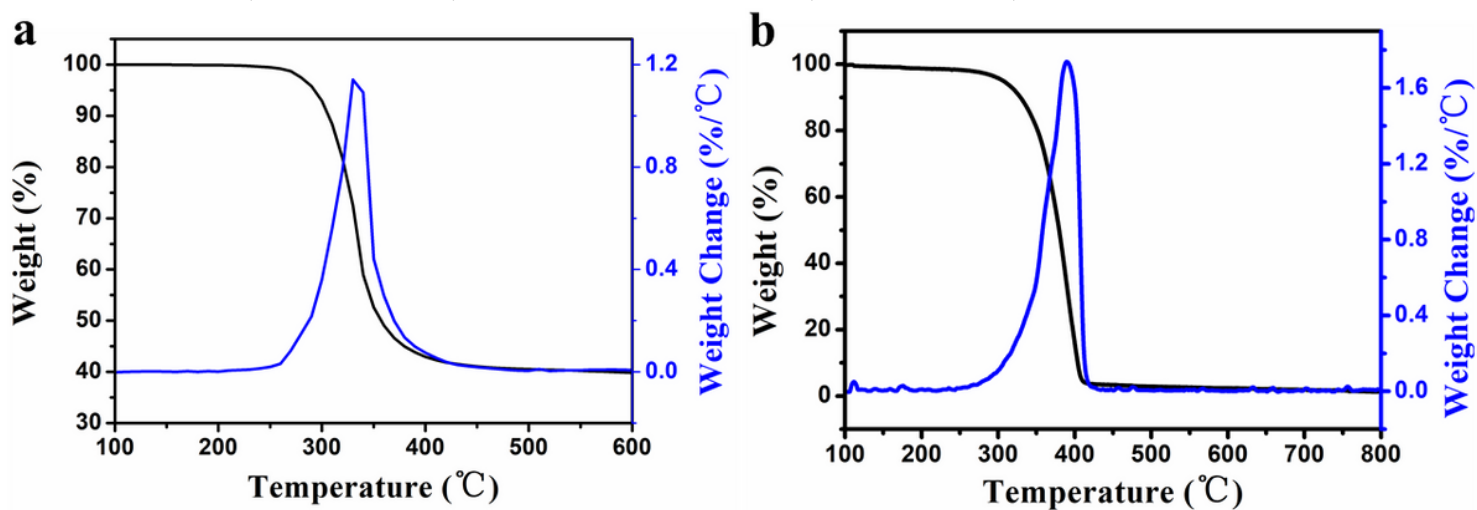


Figure 6

a-TGA curve of $(C_6H_5CH_2NH_3)_2BiCl_5$; b-TGA curve of $(C_6H_5CH_2NH_3)BiI_4$

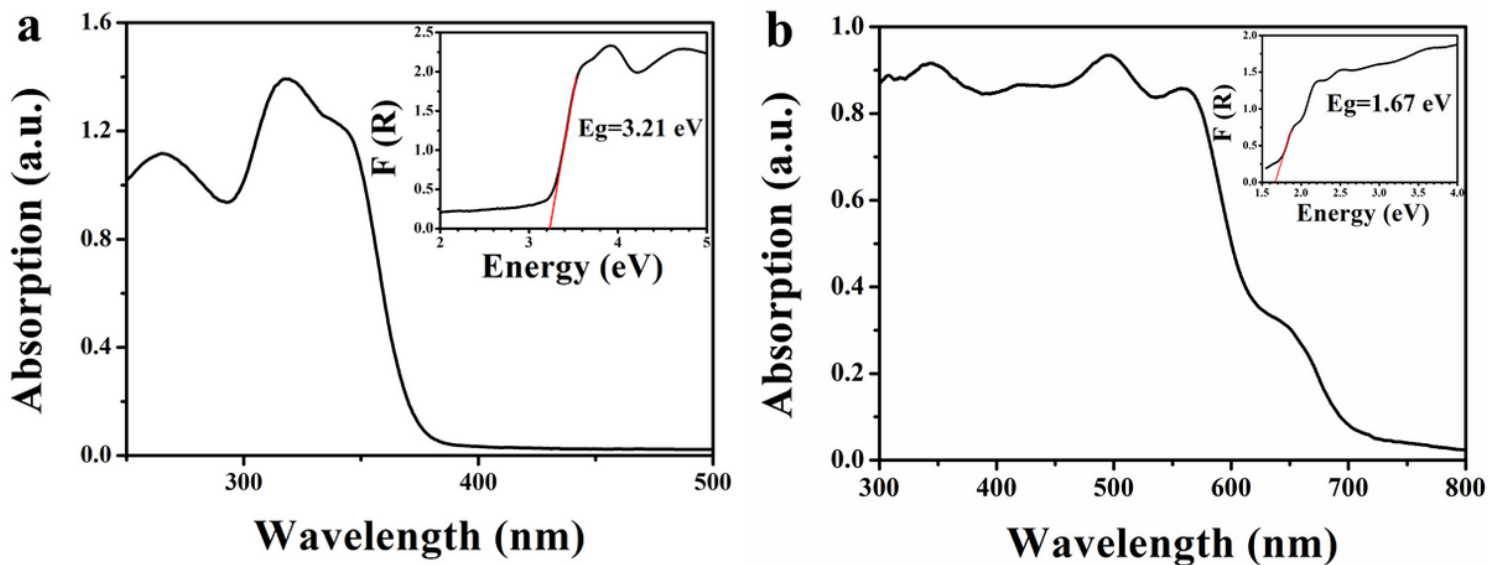


Figure 7

a-UV-vis diffuse reflectance spectroscopy plots of $(\text{C}_6\text{H}_5\text{CH}_2\text{NH}_3)_2\text{BiCl}_5$; b-UV-vis diffuse reflectance spectroscopy plots of $(\text{C}_6\text{H}_5\text{CH}_2\text{NH}_3)\text{BiI}_4$

Supplementary Files

This is a list of supplementary files associated with this preprint. Click to download.

- [SupportingInformation1.docx](#)